

## Research Article

# Expediting H<sub>2</sub> Evolution over MAPbI<sub>3</sub> with a Nonnoble Metal Cocatalyst Mo<sub>2</sub>C under Visible Light

Jinxing Yu and Xiaoxiang Xu 

Shanghai Key Lab of Chemical Assessment and Sustainability, School of Chemical Science and Engineering, Tongji University, Shanghai 200092, China

Correspondence should be addressed to Xiaoxiang Xu; xxxu@tongji.edu.cn

Received 12 March 2022; Accepted 7 May 2022; Published 28 May 2022

Copyright © 2022 Jinxing Yu and Xiaoxiang Xu. Exclusive Licensee Beijing Institute of Technology Press. Distributed under a Creative Commons Attribution License (CC BY 4.0).

Halide perovskites have been emerging as promising photocatalytic materials for H<sub>2</sub> evolution from water due to their outstanding photoelectric properties. However, the lack of proper surface reactive sites greatly hinders the photocatalytic potential of these fascinating compounds. Here, Mo<sub>2</sub>C nanoparticles have been anchored onto methylammonium lead iodide (MAPbI<sub>3</sub>) as a nonnoble metal cocatalyst to promote H<sub>2</sub> evolution reactions. The Mo<sub>2</sub>C nanoparticles have opposite zeta potential with MAPbI<sub>3</sub>, thereby electrostatically assembled onto the MAPbI<sub>3</sub> surface, i.e., Mo<sub>2</sub>C@MAPbI<sub>3</sub>. Our results show that the anchored Mo<sub>2</sub>C nanoparticles have a strong interplay with MAPbI<sub>3</sub> substrate so that photogenerated electrons of MAPbI<sub>3</sub> can be rapidly separated and transferred into Mo<sub>2</sub>C for further H<sub>2</sub> evolution reactions. Under optimal conditions, Mo<sub>2</sub>C@MAPbI<sub>3</sub> delivers exceptionally high photocatalytic performance for visible light-driven H<sub>2</sub> evolution that clearly outperforms pristine MAPbI<sub>3</sub> and Pt-deposited MAPbI<sub>3</sub>. An apparent quantum efficiency as high as 12.65% at 600 ± 40 nm has been attained for H<sub>2</sub> evolution, surpassing most of the MAPbI<sub>3</sub>-based photocatalyst reported. These results signify the usefulness and applicability of Mo<sub>2</sub>C as a new nonnoble metal-based cocatalyst in solar water splitting.

## 1. Introduction

Hydrogen is an ideal substitute for traditional fossil fuels because of its zero-carbon emissions and high energy density [1, 2]. Photocatalytic water splitting has been considered as a promising route to store solar energy into hydrogen energy [3]. Ever since photocatalysis over TiO<sub>2</sub> was reported [4], numerous photocatalysts have been explored for H<sub>2</sub> production from water, including SrTiO<sub>3</sub> [5], ZnIn<sub>2</sub>S<sub>4</sub> [6], g-C<sub>3</sub>N<sub>4</sub> [7], MOFs [8], and COFs [9] [10–16]. Recently, halide perovskites with chemical formula ABX<sub>3</sub> (A = Cs or organic cation, B = Pb<sup>2+</sup> or Sn<sup>2+</sup>, and X = Cl<sup>−</sup>, Br<sup>−</sup>, or I<sup>−</sup>) have gained great interest as photocatalysts for H<sub>2</sub> evolution reactions [17, 18]. This has been ascribed to their superior visible light absorption and high charge mobility which are strongly desired for photocatalytic reactions [19, 20]. The latter is extremely useful to inhibit charge recombination which is commonly encountered by conventional semiconductors. Although halide perovskites own many promising photoelectric properties, they are normally deficient in surface reactive sites where photocarriers

cannot be promptly transferred for surface redox reactions [21]. In addition, the extremely acidic environment that needed to stabilize halide perovskites in an aqueous solution restrains the choices of H<sub>2</sub> evolution cocatalyst that can be deposited. In this regard, the noble metal cocatalyst Pt has been introduced to promote H<sub>2</sub> evolution reactions but is still unsatisfactory probably due to the poor Pt/halide perovskite interfaces. Lately, some nonnoble metal-based cocatalysts have gained serious attention as alternatives to noble metal cocatalyst such as NiCoB [22], MoC [23], Ni<sub>3</sub>C [24], MoS<sub>2</sub> [25, 26], BP [27], and CoP [28]. However, their connections with halide perovskites are generally very weak due to structural mismatch thereby preventing fast charge collections from halide perovskites to these cocatalysts.

Mo<sub>2</sub>C, a promising low-cost electrocatalyst for H<sub>2</sub> evolution reaction, exhibits excellent electrocatalytic activity over a wide pH range thereby serving as a potential candidate cocatalyst for photocatalytic H<sub>2</sub> evolution [29–31]. More importantly, Mo<sub>2</sub>C is one of the few compounds that are stable in strong acids, rendering it an excellent alternative cocatalyst

for halide perovskites which are stabilized in strong acid during photocatalytic reactions, e.g., HBr and HI aqueous solution [32–36].

Here, take methylammonium lead iodide (MAPbI<sub>3</sub>) as an example; we deposit Mo<sub>2</sub>C onto MAPbI<sub>3</sub> as a nonnoble metal cocatalyst for photocatalytic water reduction into H<sub>2</sub>. The opposite zeta potentials between Mo<sub>2</sub>C and MAPbI<sub>3</sub> ensure firm interconnections between these two materials that favor fast charge dissociation and transfer. It is shown that the photocatalytic activities of MAPbI<sub>3</sub> are significantly boosted upon deposition of Mo<sub>2</sub>C nanoparticles with an optimal H<sub>2</sub> evolution rate as high as 1.05 mmol h<sup>-1</sup> g<sup>-1</sup>, being almost 66 times higher than pristine MAPbI<sub>3</sub>.

## 2. Experimental

**2.1. Material Synthesis.** Synthesis of Mo<sub>2</sub>C NPs: 1.0000 g of (NH<sub>4</sub>)<sub>6</sub>Mo<sub>7</sub>O<sub>24</sub>·4H<sub>2</sub>O (Aladdin, 99.0%) and 2.9154 g of glucose (Aladdin, 99.5%) were dispersed into deionized water (c.a. 80 mL) under magnetic stirring. The so-formed admixtures were sealed into a stainless autoclave (Teflon-lined, 100 mL) for hydrothermal reaction at 453 K for 12 h. A solid power precursor can be collected after centrifugation and dried in a vacuum oven. The precursor was then calcined in 5% H<sub>2</sub>/Ar at 1123 K for 3 h. The resultant product was rinsed with deionized water and desiccated for further analysis.

Synthesis of MAPbI<sub>3</sub> and MAPbI<sub>3</sub>-saturated HI/H<sub>3</sub>PO<sub>2</sub> solution: 4.6146 g PbI<sub>2</sub> (Aladdin, 99.9%) was dissolved in 25 mL HI/H<sub>3</sub>PO<sub>2</sub> (volume ratio = 4 : 1) aqueous solution. After being heated to 373 K, 1.6221 g MAI (Aladdin, 98%) was added. The so-formed solution was cooled naturally to ambient temperature as a saturation solution for MAPbI<sub>3</sub>. Black MAPbI<sub>3</sub> precipitates appeared gradually and were centrifuged and dried in a vacuum oven overnight. The saturation solution was stored for further use.

Synthesis of Mo<sub>2</sub>C@MAPbI<sub>3</sub> composites: the Mo<sub>2</sub>C@-MAPbI<sub>3</sub> composites were prepared by electrostatic self-assembling: in brief, 100 mg of MAPbI<sub>3</sub> and proper amounts of Mo<sub>2</sub>C NPs (5, 10, 15, 20, and 25 mg) were added into 10 mL MAPbI<sub>3</sub>-saturated HI/H<sub>3</sub>PO<sub>2</sub> solution, respectively. The so-formed suspensions were heated to 373 K under magnetic stirring for 30 min and cooled naturally. The precipitants obtained were denoted according to the amounts of Mo<sub>2</sub>C relative to MAPbI<sub>3</sub> as 5% Mo<sub>2</sub>C@MAPbI<sub>3</sub>, 10% Mo<sub>2</sub>C@MAPbI<sub>3</sub>, 15% Mo<sub>2</sub>C@MAPbI<sub>3</sub>, 20% Mo<sub>2</sub>C@MAPbI<sub>3</sub>, and 25% Mo<sub>2</sub>C@MAPbI<sub>3</sub>, respectively.

Synthesis of Pt/MAPbI<sub>3</sub>: appropriate amounts of H<sub>2</sub>PtCl<sub>6</sub> and 20 mg MAPbI<sub>3</sub> were added into the MAPbI<sub>3</sub>-saturated HI/H<sub>3</sub>PO<sub>2</sub> solution under magnetic stirring. The suspensions were subsequently irradiated under visible light illumination (Perfect Light, PLX-SXE300, λ ≥ 420 nm) for 30 min. The precipitants were centrifuged and collected for further analysis.

**2.2. Material Characterization.** All sample powders were analyzed by X-ray powder diffraction (XRD) techniques (Bruker D8 Focus diffractometer) for phase identifications. The morphologies of sample particles were inspected using a field-emission scanning electron microscope (FE-SEM, Hitachi S4800) and transmission electron microscope

(TEM, JEOL JEM-2100). UV-vis diffuse reflectance spectra of sample powders were acquired using a UV-vis spectrophotometer (JASCO-V750). Photoluminescence (PL) spectra were acquired on a Hitachi F-7000 fluorescence spectrometer (excitation wavelength: 520 nm). X-ray photoelectron spectroscopy (XPS) data was collected on Thermo Escalab 250. Brunauer-Emmett-Teller (BET) surface areas were analyzed using TriStar 3020. Zeta potentials were measured with a LiteSizer 500 Particle Analyzer.

**2.3. Photocatalytic Activity.** The photocatalytic hydrogen evolution reactions of prepared samples were assessed in a Labsolar-6A system (Perfect Light, China) at 293 K. Typically, 20 mg as-prepared catalyst was dispersed in 20 mL MAPbI<sub>3</sub>-saturated HI/H<sub>3</sub>PO<sub>2</sub> solution. The suspensions were sealed and evacuated (100 Pa) for 60 minutes before light illumination. A 300 W Xenon lamp coupled with a UV cutoff filter (λ ≥ 420 nm) (Perfect Light, PLX-SXE300) was used as a light source. The gas evolution during photocatalytic reaction was monitored by an online gas chromatograph (TECHCOMP, GC7900). The carrier gas is ultrapure Ar (99.999%). The photon flux of the light source was analyzed by a quantum meter (Apogee MP-300) for the determination of the apparent quantum efficiency (AQE) according to the following equation:

$$\text{AQE} = \frac{2 \times \text{mol of hydrogen production per hour}}{\text{moles of photon flux per hour}} \times 100\%. \quad (1)$$

**2.4. Photoelectrochemical Measurements.** Photoelectrodes of MAPbI<sub>3</sub> and 10% Mo<sub>2</sub>C@MAPbI<sub>3</sub> were prepared by a drop-casting method [24]. 10 mg of catalysts was dispersed into 10 mL absolute diethyl ether under magnetic stirring to form suspensions. The suspensions were then dropped onto fluorine-doped tin oxide (FTO) glass and dried naturally. The deposited FTO glass was calcined at 353 K for 30 min under N<sub>2</sub> atmosphere to improve the adhesion between sample powders and glass. The so-formed electrode was used as the working electrode. Photoelectrochemical (PEC) measurements were carried out in a three-electrode configuration which was controlled by a Zahner electrochemical workstation. The counter and reference electrodes were Pt foil and Ag/AgCl electrodes, respectively. MAPbI<sub>3</sub>-saturated aqueous HI/H<sub>3</sub>PO<sub>2</sub> solution was used as the electrolyte which was degassed with nitrogen atmosphere for 30 min before the use. The light source was the same as photocatalytic experiment.

## 3. Results and Discussion

**3.1. Phase Compositions.** The as-prepared Mo<sub>2</sub>C, MAPbI<sub>3</sub>, and Mo<sub>2</sub>C@MAPbI<sub>3</sub> powders were analyzed by XRD as shown in Figure 1(a). The as-prepared Mo<sub>2</sub>C and MAPbI<sub>3</sub> powders have identical XRD patterns with those of standard ones, indicating the successful formation of single-phase compounds [26, 33]. The Mo<sub>2</sub>C@MAPbI<sub>3</sub> powders contain both reflections from Mo<sub>2</sub>C and MAPbI<sub>3</sub>, suggesting the coexistence of both compounds. For instance, the main reflection of Mo<sub>2</sub>C around 39° can be easily identified for Mo<sub>2</sub>C@MAPbI<sub>3</sub> powders whose intensity monotonically increased with the amounts of Mo<sub>2</sub>C

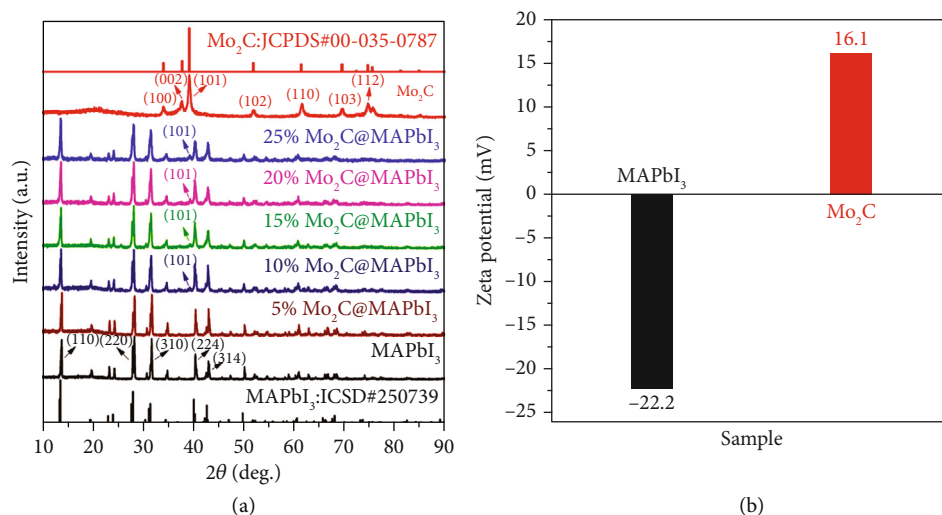


FIGURE 1: (a) XRD patterns of the synthesized Mo<sub>2</sub>C, MAPbI<sub>3</sub>, and Mo<sub>2</sub>C@MAPbI<sub>3</sub> composites. (b) Zeta potentials of MAPbI<sub>3</sub> and Mo<sub>2</sub>C.

introduced. The facile formation of Mo<sub>2</sub>C@MAPbI<sub>3</sub> composites can be rationalized by the opposite zeta potentials of Mo<sub>2</sub>C and MAPbI<sub>3</sub> [37], as shown in Figure 1(b). The strong coulombic force between Mo<sub>2</sub>C and MAPbI<sub>3</sub> would enable firm interconnections among their particles which are further investigated by microscopic analysis.

**3.2. Microstructures.** The FE-SEM images of Mo<sub>2</sub>C, MAPbI<sub>3</sub>, and Mo<sub>2</sub>C@MAPbI<sub>3</sub> are displayed in Figure S1, Figure S2, and Figure 2. As shown in Figure S1, the as-prepared Mo<sub>2</sub>C comprises spherical nanoparticles with a size of about 50 nm. The pristine MAPbI<sub>3</sub>, however, is composed of bulky particles of 10~20 micrometers with a smooth surface (Figure S2). Further loading Mo<sub>2</sub>C onto MAPbI<sub>3</sub> results in intriguing microstructures where small Mo<sub>2</sub>C granules adhere tightly to the surface of MAPbI<sub>3</sub> (Figures 2(a) and 2(b)). The dispersion of Mo<sub>2</sub>C at the surface of MAPbI<sub>3</sub> is homogeneous as indicated by EDS elemental mapping analysis (Figure 2(c)). These observations are fully consistent with previous deductions that there are strong interconnections between Mo<sub>2</sub>C and MAPbI<sub>3</sub>. Such a strong interplay is highly beneficial for charge migration across the interfaces and highly desired for photocatalytic reactions [38, 39]. The corresponding EDS spectra of 10% Mo<sub>2</sub>C@MAPbI<sub>3</sub> composites are shown in Figure S3 in which the content of Pb, I, and Mo is consistent with nominal compositions (Table S1). The Mo<sub>2</sub>C@MAPbI<sub>3</sub> composites were further inspected under TEM conditions. Figure S4a illustrates the TEM image of the 10% Mo<sub>2</sub>C@MAPbI<sub>3</sub> composites. Unlike MAPbI<sub>3</sub> which normally has a smooth surface, 10% Mo<sub>2</sub>C@MAPbI<sub>3</sub> clearly has small nanoparticles on its surfaces. HRTEM image suggests that these nanoparticles belong to Mo<sub>2</sub>C according to the lattice fringe of 0.228 nm, which correspond well with the (101) planes of hexagonal Mo<sub>2</sub>C (Figure S4b) [40]. It is worth noting that Mo<sub>2</sub>C nanoparticles attached to MAPbI<sub>3</sub> in a face-to-face manner, confirming the strong linkage between Mo<sub>2</sub>C and MAPbI<sub>3</sub> [41, 42]. Thereby, we have successfully fabricated Mo<sub>2</sub>C@MAPbI<sub>3</sub> composites with intimate contact between

different moieties. As a result, the specific surface area of Mo<sub>2</sub>C@MAPbI<sub>3</sub> composites is much higher than that of pristine MAPbI<sub>3</sub> (0.1 m<sup>2</sup>/g) due to the presence of Mo<sub>2</sub>C nanoparticles with high specific surface area (12.11 m<sup>2</sup>/g) (Figure S5, Table S2) [43].

**3.3. UV-vis DRS Spectra.** The light absorption properties of pristine Mo<sub>2</sub>C, MAPbI<sub>3</sub>, and Mo<sub>2</sub>C@MAPbI<sub>3</sub> composites were further studied by the UV-vis diffuse reflectance spectra (UV-vis DRS). As shown in Figure 3, bare Mo<sub>2</sub>C nanoparticles demonstrate excellent light absorption capacity from 200 to 900 nm, being consistent with the black color of Mo<sub>2</sub>C [44]. MAPbI<sub>3</sub> also maintains significant visible light absorption with a sharp absorption edge approaching 840 nm. Thanks to the optical properties of Mo<sub>2</sub>C and MAPbI<sub>3</sub>, Mo<sub>2</sub>C@MAPbI<sub>3</sub> composites all have intense absorption in the visible light region (400 nm~800 nm). Their absorption tails above 850 nm increase along with the content of Mo<sub>2</sub>C in the samples, as frequently observed in semiconductor composites [45].

**3.4. XPS Spectra.** To further explore the interplay between Mo<sub>2</sub>C and MAPbI<sub>3</sub>, the surface state of Mo<sub>2</sub>C@MAPbI<sub>3</sub> composites was investigated by XPS technique and was compared with pristine Mo<sub>2</sub>C and MAPbI<sub>3</sub>. Figure 4(a) shows the survey scan of all samples in which signals of constituent elements of I, Pb, Mo, and C can be clearly identified. The Pb 4f state of pristine MAPbI<sub>3</sub> contains two peaks around 142.34 eV and 137.44 eV, corresponding to Pb 4f<sub>5/2</sub> and Pb 4f<sub>7/2</sub> state of Pb<sup>2+</sup> species, respectively (Figure 4(b)) [46]. These peaks, however, are clearly shifted to higher binding energy when attaching Mo<sub>2</sub>C to MAPbI<sub>3</sub>, suggesting MAPbI<sub>3</sub> loses electron after Mo<sub>2</sub>C anchorage. A similar phenomenon is also observed in the I 3d state where spin-orbital pair of I<sup>-</sup> species blue shifts approximately 0.31 eV after the formation of Mo<sub>2</sub>C@MAPbI<sub>3</sub> composites (Figure 4(c)). In contrast, the Mo 3d state of Mo<sub>2</sub>C@MAPbI<sub>3</sub> composites red shifts about 0.45 eV compared with pristine Mo<sub>2</sub>C (Figure 4(d)). These results consistently suggest that there



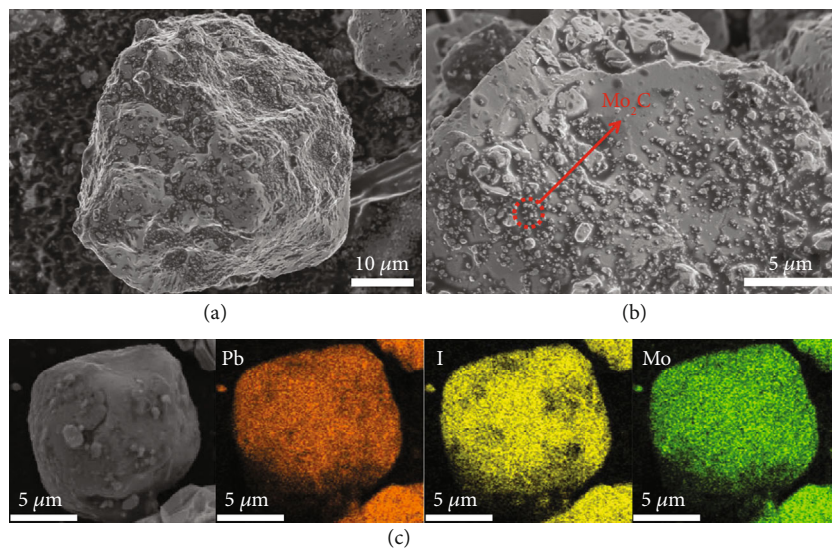


FIGURE 2: (a, b) SEM images of 10% Mo<sub>2</sub>C@MAPbI<sub>3</sub>. (c) The corresponding EDS elemental mapping of 10% Mo<sub>2</sub>C@MAPbI<sub>3</sub>.

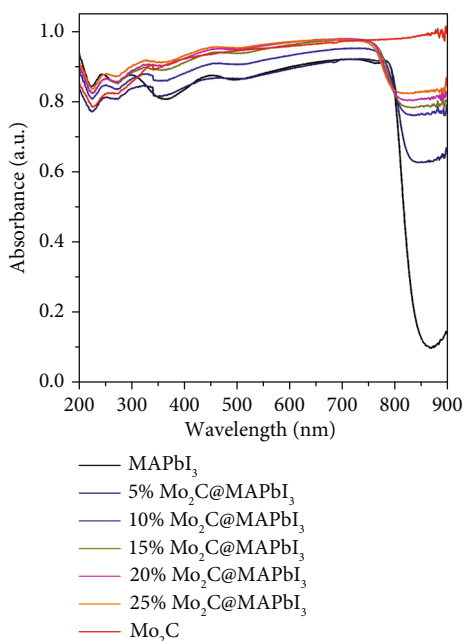


FIGURE 3: UV-vis DRS spectra of Mo<sub>2</sub>C, MAPbI<sub>3</sub>, and Mo<sub>2</sub>C@MAPbI<sub>3</sub> composites.

are strong interconnections between Mo<sub>2</sub>C and MAPbI<sub>3</sub>, and Mo<sub>2</sub>C can accept electrons from MAPbI<sub>3</sub> [47]. It is noteworthy that the Mo 3d state contains two distinct spin-orbital pairs. The pair at a higher binding energy side, i.e., 233.04 and 235.95 eV, is assignable to Mo 3d<sub>5/2</sub> and Mo 3d<sub>3/2</sub> states of Mo<sup>6+</sup> in MoO<sub>3</sub> while the one at the lower binding energy side belongs to Mo<sup>2+</sup> of Mo<sub>2</sub>C. These results imply that Mo<sub>2</sub>C is slightly oxidized at the surface which is also noticed in the previous reports [48, 49].

**3.5. Photocatalytic Properties.** The photocatalytic activity of as-prepared samples was evaluated by comparing their H<sub>2</sub> evolution in MAPbI<sub>3</sub>-saturated HI/H<sub>3</sub>PO<sub>2</sub> solution under visible light illumination ( $\lambda \geq 420$  nm). The system for the experiments was examined first by removing one of the following components including photocatalyst, light, and water during photocatalytic experiments. No H<sub>2</sub> signal can be detected under these circumstances; therefore, the system is free of spontaneous H<sub>2</sub> evolution reactions. However, H<sub>2</sub> evolution was recorded upon illuminating sample powders with MAPbI<sub>3</sub>-saturated HI/H<sub>3</sub>PO<sub>2</sub> solution, affirming true photocatalytic processes. The H<sub>2</sub> evolution of all samples as a function of illumination time is summarized in Figure 5(a). Pristine MAPbI<sub>3</sub> is characterized by a poor H<sub>2</sub> evolution activity and produces only 40.14 μmol/g H<sub>2</sub> for 2.5 h. This can be rationalized by the lack of proper surface reaction sites so that photogenerated electrons cannot be promptly transferred at the surface for water reduction reactions [50]. Strikingly, H<sub>2</sub> evolution is considerably boosted when Mo<sub>2</sub>C nanoparticles are loaded onto MAPbI<sub>3</sub>. Among all Mo<sub>2</sub>C@MAPbI<sub>3</sub> composites, 10% Mo<sub>2</sub>C@MAPbI<sub>3</sub> exhibited the highest H<sub>2</sub> evolution activity (1054 μmol g<sup>-1</sup> h<sup>-1</sup>), nearly 66-fold higher than that of pristine MAPbI<sub>3</sub> (16 μmol g<sup>-1</sup> h<sup>-1</sup>). It is worth noting that pristine Mo<sub>2</sub>C is completely inactive for H<sub>2</sub> evolution under identical conditions, indicating that Mo<sub>2</sub>C is a cocatalyst to promote water reduction reactions [51]. The average H<sub>2</sub> evolution rates of all samples are illustrated in Figure 5(b). A volcano-type profile can be noticed for the H<sub>2</sub> evolution rates vs. Mo<sub>2</sub>C content in the Mo<sub>2</sub>C@MAPbI<sub>3</sub> composites. This can be attributed to the aggregation of Mo<sub>2</sub>C that decreases the active surface sites and/or blocks light penetration [52]. The optimal Mo<sub>2</sub>C content is found to be 10% and is adopted for the measurement of apparent quantum efficiency (AQE). The AQE of 10% Mo<sub>2</sub>C@MAPbI<sub>3</sub> is summarized in Figure 5(c). It can be seen from Figure 5(c) that

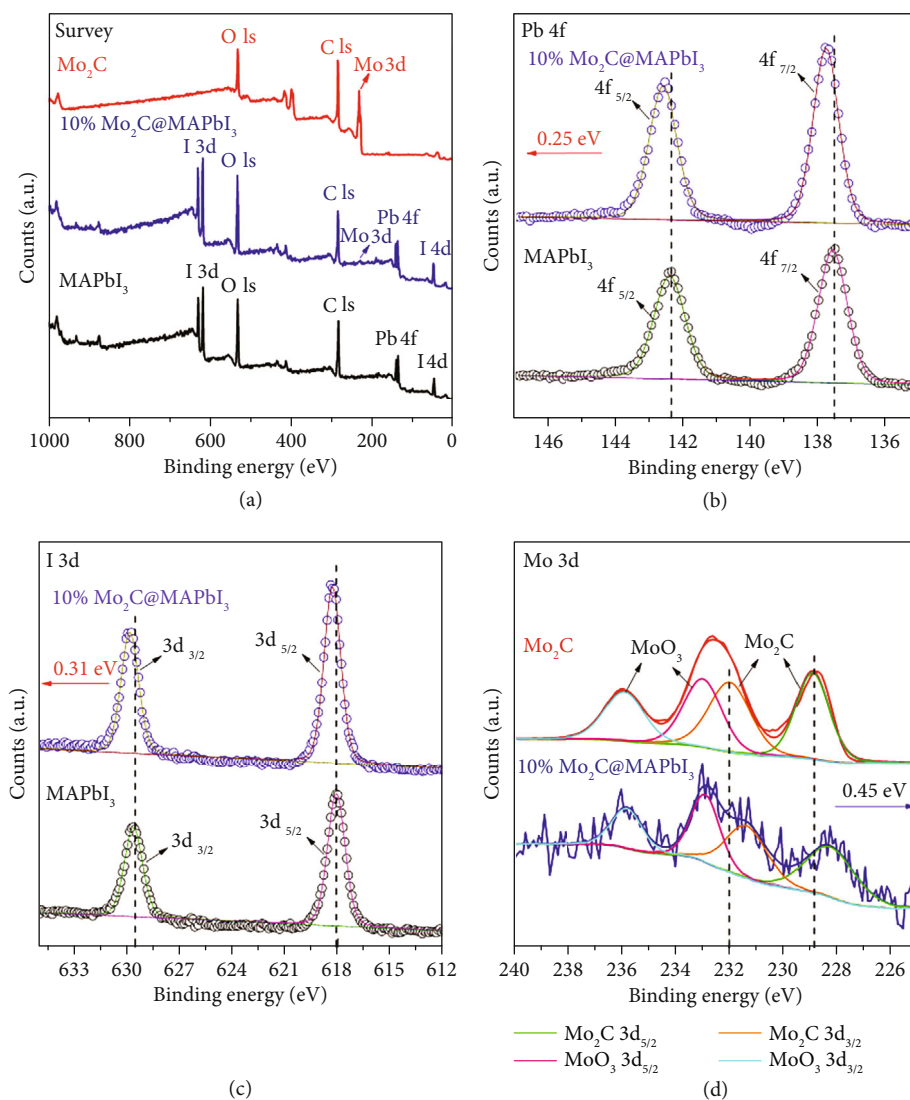


FIGURE 4: XPS spectra of Mo<sub>2</sub>C, MAPbI<sub>3</sub>, and 10% Mo<sub>2</sub>C@MAPbI<sub>3</sub>: (a) survey spectrum and high-resolution XPS spectra of (b) Pb 4f, (c) I 3d, and (d) Mo 3d.

10% Mo<sub>2</sub>C@MAPbI<sub>3</sub> maintains a high AQE (>10%) at all measurement points, verifying the exceptionally high photocatalytic activity for H<sub>2</sub> evolution from water. On the other hand, the superior performance of Mo<sub>2</sub>C@MAPbI<sub>3</sub> composites can also be realized by comparing their H<sub>2</sub> evolution activity with those of Pt-deposited MAPbI<sub>3</sub> (Figure S6). It can be seen from Figure S6 that the Pt-deposited MAPbI<sub>3</sub> has a much lower H<sub>2</sub> evolution activity than Mo<sub>2</sub>C@MAPbI<sub>3</sub> even though the Pt content has been optimized. In addition, Mo<sub>2</sub>C@MAPbI<sub>3</sub> composites also deliver a much better H<sub>2</sub> evolution activity than most of the MAPbI<sub>3</sub>-based photocatalysts reported in the literatures as summarized in Table S3. After continuous six cycles of usage, Mo<sub>2</sub>C@MAPbI<sub>3</sub> can still maintain most of its initial activity, indicative of good stability (Figure 5(d)). Besides, XRD analysis suggests that the crystal structure and the compositions of Mo<sub>2</sub>C@MAPbI<sub>3</sub> composites have no discernable change before and after photocatalytic experiments, confirming again its good stability (Figure S7).

**3.6. Photoluminescence Spectra and Photoelectrochemical Analysis.** Given the superior photocatalytic activity of Mo<sub>2</sub>C@MAPbI<sub>3</sub> composites, the charge separation conditions of MAPbI<sub>3</sub> in response to Mo<sub>2</sub>C loading have been investigated. Firstly, the steady-state photoluminescence (PL) spectra of 10% Mo<sub>2</sub>C@MAPbI<sub>3</sub> and MAPbI<sub>3</sub> have been collected. Both samples show an intense PL signal around 790 nm, corresponding to the band edge emission of radiative-type charge recombination [24]. It is clear from Figure 6(a) that this PL signal is considerably reduced when loading Mo<sub>2</sub>C onto MAPbI<sub>3</sub>, indicating reduced radiative-type charge recombination in the composites [53–55]. In addition, photocurrent measurements suggest that 10% Mo<sub>2</sub>C@MAPbI<sub>3</sub> owns a much higher photocurrent than pristine MAPbI<sub>3</sub> under the same electric bias, confirming the ameliorated charge separation conditions in Mo<sub>2</sub>C@MAPbI<sub>3</sub> composites (Figure 6(b)) [56]. On the other hand, electrochemical impedance spectra (EIS) suggest that the

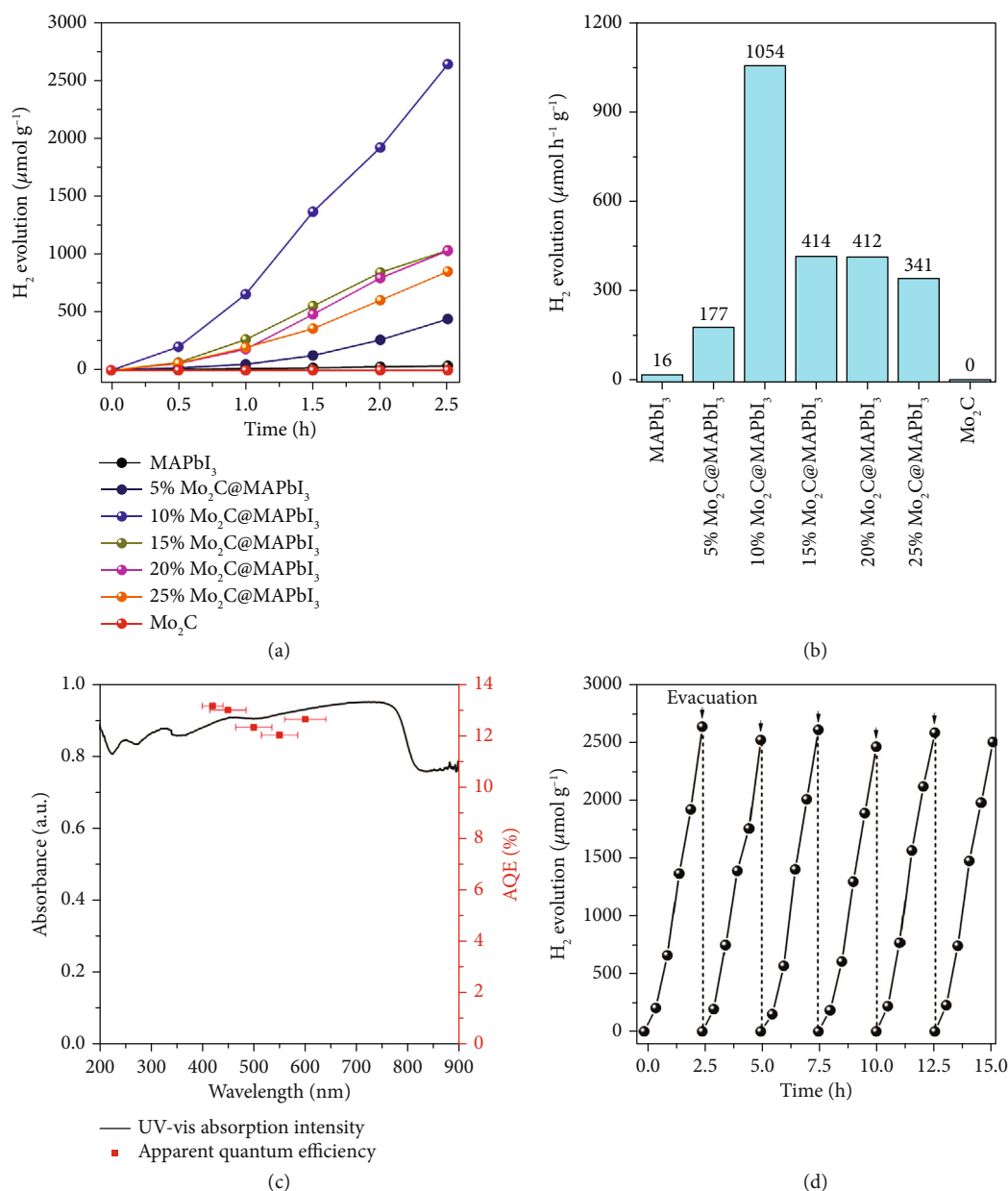


FIGURE 5: (a) Temporal photocatalytic hydrogen evolution of  $\text{Mo}_2\text{C}$ ,  $\text{MAPbI}_3$ , and  $\text{Mo}_2\text{C}@ \text{MAPbI}_3$  composites under visible light ( $\lambda \geq 420 \text{ nm}$ ) illumination; (b) average hydrogen production rate for different samples; (c) action spectra of 10%  $\text{Mo}_2\text{C}@ \text{MAPbI}_3$ ; (d) cycling usage of 10%  $\text{Mo}_2\text{C}@ \text{MAPbI}_3$  for  $\text{H}_2$  evolution, the system was evacuated for every 2.5 h.

interfacial charge transfer resistance is significantly reduced after loading  $\text{Mo}_2\text{C}$  onto  $\text{MAPbI}_3$ , verifying the role of  $\text{Mo}_2\text{C}$  as a cocatalyst to expedite interfacial charge transfer (Figure 6(c)) [57, 58]. These results consistently suggest that  $\text{Mo}_2\text{C}$  serves as a good cocatalyst for  $\text{MAPbI}_3$  which not only accelerates charge separation in the bulk of  $\text{MAPbI}_3$  but also promotes interfacial charge transfer at the surface of  $\text{MAPbI}_3$ . The flat-band potential of  $\text{MAPbI}_3$  is determined to be  $-0.48 \text{ V}$  (vs. NHE) via a Mott-Schottky analysis (Figure S8b) [59, 60]. Combining the bandgap value ( $\sim 1.51 \text{ eV}$ ) from Tauc plot analysis of  $\text{MAPbI}_3$  (Figure S8a), the band edge positions of  $\text{MAPbI}_3$  can be roughly deduced. Figure 6(d)

schematically illustrates the charge migration and reaction pathways in  $\text{Mo}_2\text{C}@ \text{MAPbI}_3$  composites.  $\text{MAPbI}_3$  can be readily excited by visible light photons to generate electron-hole pairs [61, 62]. The presence of  $\text{Mo}_2\text{C}$  at the surface of  $\text{MAPbI}_3$  promotes the dissociation of electron-hole pairs and collects electrons from  $\text{MAPbI}_3$  [63, 64]. The spatially separated charges can then participate in the surface redox reactions, i.e., water reduction into  $\text{H}_2$  over  $\text{Mo}_2\text{C}$  and  $\text{I}^-$  oxidation into  $\text{I}_3^-$  over  $\text{MAPbI}_3$ . The detailed mechanism of how charges are separated and transferred can be explored by theoretical calculations (e.g., DFT) and will be our future work.

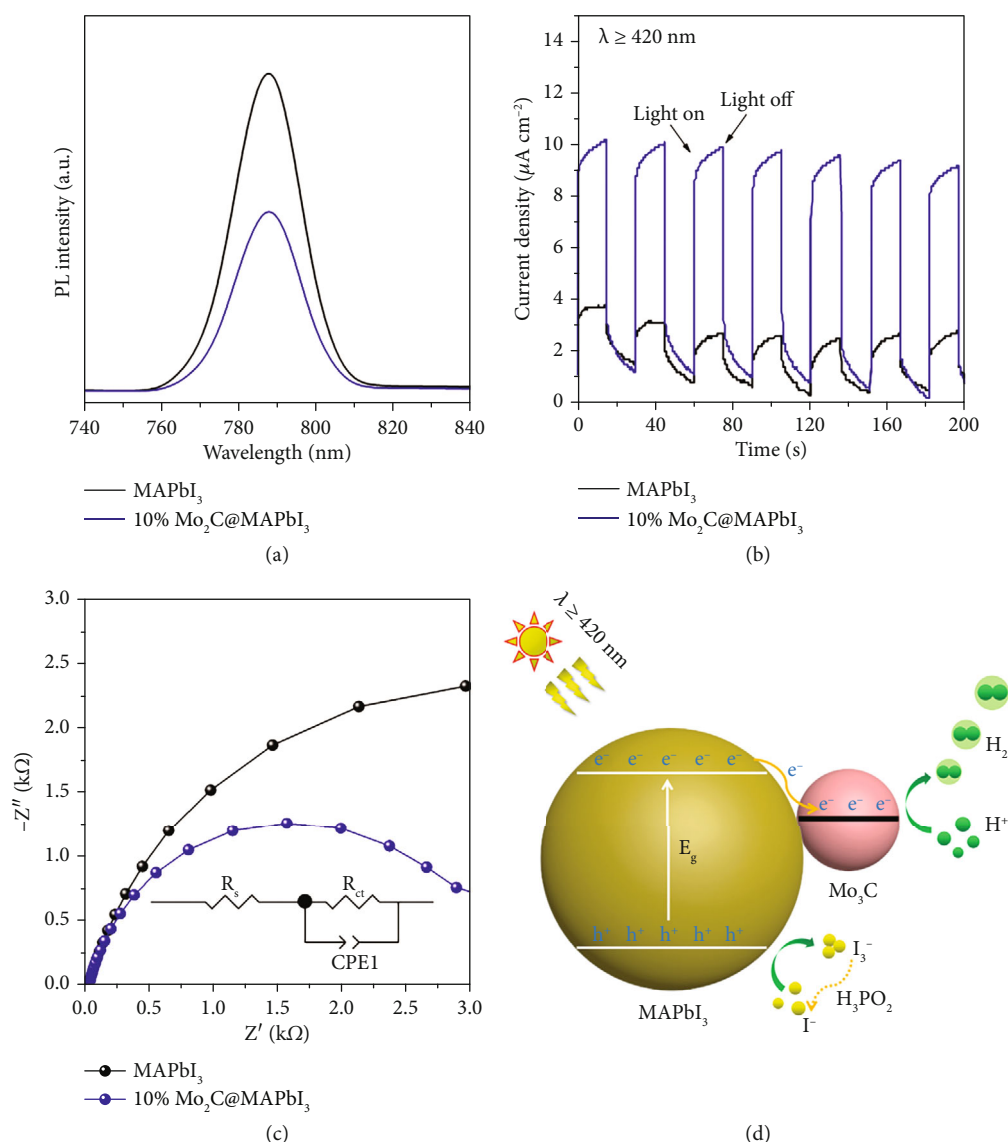


FIGURE 6: (a) Steady-state PL spectra of 10% Mo<sub>2</sub>C@MAPbI<sub>3</sub> and MAPbI<sub>3</sub>; (b) transient photocurrent responses of 10% Mo<sub>2</sub>C@MAPbI<sub>3</sub> and MAPbI<sub>3</sub> under visible light ( $\lambda \geq 420$  nm) irradiation; (c) Nyquist plot of 10% Mo<sub>2</sub>C@MAPbI<sub>3</sub> and MAPbI<sub>3</sub> photoelectrodes at open-circuit voltage under visible light irradiation conditions with a frequency range from 100 kHz to 0.1 Hz at 10 mV, the equivalent circuit diagram is shown as inset; (d) mechanistic illustration of band alignments of Mo<sub>2</sub>C@MAPbI<sub>3</sub>.

#### 4. Conclusions

We have successfully loaded Mo<sub>2</sub>C nanoparticles onto MAPbI<sub>3</sub> by an electrostatic assembly method to fabricate Mo<sub>2</sub>C@MAPbI<sub>3</sub> composites. The Mo<sub>2</sub>C nanoparticles are homogeneously and tightly anchored at the surface of MAPbI<sub>3</sub>. Thanks to the strong interconnections between Mo<sub>2</sub>C and MAPbI<sub>3</sub>, Mo<sub>2</sub>C@MAPbI<sub>3</sub> composites exhibit superior photocatalytic activity for H<sub>2</sub> evolution from water which clearly surpasses pristine MAPbI<sub>3</sub> and Pt-deposited MAPbI<sub>3</sub> under the same testing conditions. Under optimal conditions, Mo<sub>2</sub>C@MAPbI<sub>3</sub> composites achieve a high AQE for H<sub>2</sub> evolution (>10%) from 420 nm to 600 nm. Further analysis suggests that Mo<sub>2</sub>C nanoparticles not only facilitate charge separation in MAPbI<sub>3</sub> but also substantially

expedite interfacial charge transfer for water reduction reactions. These findings justify the Mo<sub>2</sub>C as an efficient nonnoble metal cocatalyst for halide perovskite photocatalysts that work under a highly acidic environment.

#### Data Availability

The data that support the findings of this study are available from the corresponding author upon reasonable request.

#### Conflicts of Interest

The authors declare that there is no conflict of interest regarding the publication of this article.



## Authors' Contributions

J.Y. conducted the experiments and analyzed the data. X.X. wrote the manuscript and supervised the project.

## Acknowledgments

We are grateful for the financial support from the National Natural Science Foundation of China (Grant Nos. 51972233 and 52172225), the Natural Science Foundation of Shanghai (Grant No. 19ZR1459200), the Science and Technology Commission of Shanghai Municipality (19DZ2271500), and the Fundamental Research Funds for the Central Universities.

## Supplementary Materials

SEM images of  $\text{Mo}_2\text{C}$  and  $\text{MAPbI}_3$ ; EDX spectrum of 10%  $\text{Mo}_2\text{C}@ \text{MAPbI}_3$ ; TEM and HRTEM image of 10%  $\text{Mo}_2\text{C}@ \text{MAPbI}_3$ ; nitrogen adsorption-desorption isotherm and pore size distribution of as-prepared samples; temporal photocatalytic hydrogen evolution for  $\text{MAPbI}_3$  loaded with different amounts of Pt under visible light ( $\lambda \geq 420 \text{ nm}$ ) illumination; XRD patterns of 10%  $\text{Mo}_2\text{C}@ \text{MAPbI}_3$  before and after the photocatalytic cyclic test; the EDS results of Mo, Pb, and I in the 10%  $\text{Mo}_2\text{C}@ \text{MAPbI}_3$ ; BET surface area of as-prepared samples; the comparison of photocatalytic  $\text{H}_2$  evolution performances over recently reported metal halide perovskite. (*Supplementary Materials*)

## References

- [1] Y. X. Zhao, S. Zhang, R. Shi, G. I. N. Waterhouse, J. W. Tang, and T. R. Zhang, "Two-dimensional photocatalyst design: a critical review of recent experimental and computational advances," *Materials Today*, vol. 34, pp. 78–91, 2020.
- [2] Z. Zhu, C. T. Kao, B. H. Tang, W. C. Chang, and R. J. Wu, "Efficient hydrogen production by photocatalytic water-splitting using Pt-doped  $\text{TiO}_2$  hollow spheres under visible light," *Ceramics International*, vol. 42, no. 6, pp. 6749–6754, 2016.
- [3] Q. Wang, L. X. Zhang, B. Li, H. M. Zhu, and J. L. Shi, "3D interconnected nanoporous  $\text{Ta}_3\text{N}_5$  films for photoelectrochemical water splitting: thickness-controlled synthesis and insights into stability," *Science China Materials*, vol. 64, no. 8, pp. 1876–1888, 2021.
- [4] A. Kudo and Y. Miseki, "Heterogeneous photocatalyst materials for water splitting," *Chemical Society Reviews*, vol. 38, no. 1, pp. 253–278, 2009.
- [5] H. Nishiyama, T. Yamada, M. Nakabayashi et al., "Photocatalytic solar hydrogen production from water on a 100- $\text{m}^2$  scale," *Nature*, vol. 598, no. 7880, pp. 304–307, 2021.
- [6] G. C. Zuo, Y. T. Wang, W. L. Teo et al., "Ultrathin  $\text{ZnIn}_2\text{S}_4$  Nanosheets anchored on  $\text{Ti}_3\text{C}_2\text{T}_x$  MXene for photocatalytic  $\text{H}_2$  Evolution," *Angewandte Chemie International Edition*, vol. 132, no. 28, pp. 11383–11388, 2020.
- [7] Y. P. Xing, X. K. Wang, S. H. Hao et al., "Recent advances in the improvement of g- $\text{C}_3\text{N}_4$  based photocatalytic materials," *Chinese Chemical Letters*, vol. 32, no. 1, pp. 13–20, 2021.
- [8] Y. Shi, A. F. Yang, C. S. Cao, and B. Zhao, "Applications of MOFs: recent advances in photocatalytic hydrogen production from water," *Coordination Chemistry Reviews*, vol. 390, pp. 50–75, 2019.
- [9] L. Stegbauer, K. Schwinghammer, and B. V. Lotsch, "A hydrazone-based covalent organic framework for photocatalytic hydrogen production," *Chemical Science*, vol. 5, no. 7, pp. 2789–2793, 2014.
- [10] J. Guo, Y. Wan, Y. F. Zhu, M. T. Zhao, and Z. Y. Tang, "Advanced photocatalysts based on metal nanoparticle/metal-organic framework composites," *Nano Research*, vol. 14, no. 7, pp. 2037–2052, 2021.
- [11] J. J. Foo, S. F. Ng, and W. J. Ong, "Dimensional heterojunction design: the rising star of 2D bismuth-based nanostructured photocatalysts for solar-to-chemical conversion," *Nano Research*, pp. 1–54, 2022.
- [12] Q. Zhong, Y. Li, and G. K. Zhang, "Two-dimensional MXene-based and MXene-derived photocatalysts: recent developments and perspectives," *Chemical Engineering Journal*, vol. 409, article 128099, 2021.
- [13] S. F. Ng, J. J. Foo, and W. J. Ong, "Solar-powered chemistry: engineering low-dimensional carbon nitride-based nanostructures for selective  $\text{CO}_2$  conversion to  $\text{C}_1$ - $\text{C}_2$  products," *Info*, vol. 4, article e12279, 2022.
- [14] P. Niu, J. J. Dai, X. J. Zhi, Z. H. Xia, S. L. Wang, and L. Li, "Photocatalytic overall water splitting by graphitic carbon nitride," *Info*, vol. 3, no. 9, pp. 931–961, 2021.
- [15] Z. S. Zhang, X. Ding, X. G. Yang, W. G. Tu, L. Wang, and Z. G. Zou, "Shedding light on  $\text{CO}_2$ : catalytic synthesis of solar methanol," *EcoMat*, vol. 3, no. 1, article e12078, 2021.
- [16] W. J. Zhang, D. Ma, J. Pérez-Ramírez, and Z. P. Chen, "Recent progress in materials exploration for thermocatalytic, photocatalytic, and integrated photothermocatalytic  $\text{CO}_2$ -to-fuel conversion," *Advanced Energy and Sustainability Research*, vol. 3, no. 2, article 2100169, 2022.
- [17] S. Park, S. Choi, S. Kim, and K. T. Nam, "Metal halide perovskites for solar fuel production and photoreactions," *Journal of Physical Chemistry Letters*, vol. 12, no. 34, pp. 8292–8301, 2021.
- [18] J. Q. Luo, W. W. Zhang, H. B. Yang et al., "Halide perovskite composites for photocatalysis: a mini review," *EcoMat*, vol. 3, no. 1, article e12079, 2021.
- [19] Y. X. Zhang, Y. C. Liu, Z. Yang, and S. Z. Liu, "High-quality perovskite  $\text{MAPbI}_3$  single crystals for broad-spectrum and rapid response integrate photodetector," *Journal of Energy Chemistry*, vol. 27, no. 3, pp. 722–727, 2018.
- [20] S. Park, W. J. Chang, C. W. Lee, S. Park, H. Y. Ahn, and K. T. Nam, "Photocatalytic hydrogen generation from hydriodic acid using methylammonium lead iodide in dynamic equilibrium with aqueous solution," *Nature Energy*, vol. 2, no. 1, pp. 1–8, 2017.
- [21] M. Y. Wang, Y. P. Zuo, J. L. Wang et al., "Remarkably enhanced hydrogen generation of organolead halide perovskites via piezocatalysis and photocatalysis," *Advanced Energy Materials*, vol. 9, no. 37, article 1901801, 2019.
- [22] L. X. Jiang, Y. M. Guo, S. P. Qi et al., "Amorphous  $\text{NiCoB}$ -coupled  $\text{MAPbI}_3$  for efficient photocatalytic hydrogen evolution," *Dalton Transactions*, vol. 50, no. 48, pp. 17960–17966, 2021.
- [23] T. T. Zhang, J. F. Yu, J. Y. Huang, S. N. Lan, Y. B. Lou, and J. X. Chen, " $\text{MoC}/\text{MAPbI}_3$  hybrid composites for efficient photocatalytic hydrogen evolution," *Dalton Transactions*, vol. 50, no. 31, pp. 10860–10866, 2021.



- [24] Z. J. Zhao, J. J. Wu, Y. Z. Zheng, N. Li, X. T. Li, and X. Tao, "Ni<sub>3</sub>C-decorated MAPbI<sub>3</sub> as visible-light photocatalyst for H<sub>2</sub> evolution from HI splitting," *ACS Catalysis*, vol. 9, no. 9, pp. 8144–8152, 2019.
- [25] F. Wang, X. Y. Liu, Z. G. Zhang, and S. X. Min, "A noble-metal-free MoS<sub>2</sub> nanosheet-coupled MAPbI<sub>3</sub> photocatalyst for efficient and stable visible-light-driven hydrogen evolution," *Chemical Communications*, vol. 56, no. 22, pp. 3281–3284, 2020.
- [26] W. H. Guan, Y. Li, Q. X. Zhong et al., "Fabricating MAPbI<sub>3</sub>/MoS<sub>2</sub> composites for improved photocatalytic performance," *Nano Letters*, vol. 21, no. 1, pp. 597–604, 2021.
- [27] R. Li, X. T. Li, J. J. Wu et al., "Few-layer black phosphorus-on-MAPbI<sub>3</sub> for superb visible-light photocatalytic hydrogen evolution from HI splitting," *Applied Catalysis B: Environmental*, vol. 259, article 118075, 2019.
- [28] C. Cai, Y. Teng, J. H. Wu et al., "In situ photosynthesis of an MAPbI<sub>3</sub>/CoP hybrid heterojunction for efficient photocatalytic hydrogen evolution," *Advanced Functional Materials*, vol. 30, no. 35, article 2001478, 2020.
- [29] S. S. Yang, Y. W. Wang, H. J. Zhang et al., "Unique three-dimensional Mo<sub>2</sub>[email protected]<sub>2</sub> heterojunction nanostructure with S vacancies as outstanding all-pH range electrocatalyst for hydrogen evolution," *Journal of Catalysis*, vol. 371, pp. 20–26, 2019.
- [30] Y. Qiu, Z. L. Wen, C. R. Jiang et al., "Rational design of atomic layers of Pt anchored on Mo<sub>2</sub>C nanorods for efficient hydrogen evolution over a wide pH range," *Small*, vol. 15, no. 14, article 1900014, 2019.
- [31] M. C. Weidman, D. V. Esposito, Y. C. Hsu, and J. G. Chen, "Comparison of electrochemical stability of transition metal carbides (WC, W<sub>2</sub>C, Mo<sub>2</sub>C) over a wide pH range," *Journal of Power Sources*, vol. 202, pp. 11–17, 2012.
- [32] D. M. Ruan, M. Fujitsuka, and T. Majima, "Exfoliated Mo<sub>2</sub>C nanosheets hybridized on CdS with fast electron transfer for efficient photocatalytic H<sub>2</sub> production under visible light irradiation," *Applied Catalysis B: Environmental*, vol. 264, article 118541, 2020.
- [33] X. Z. Yue, S. S. Yi, R. W. Wang, Z. T. Zhang, and S. L. Qiu, "A novel architecture of dandelion-like Mo<sub>2</sub>C/TiO<sub>2</sub> heterojunction photocatalysts towards high-performance photocatalytic hydrogen production from water splitting," *Journal of Materials Chemistry A*, vol. 5, no. 21, pp. 10591–10598, 2017.
- [34] X. H. Ma, C. J. Ren, H. D. Li et al., "A novel noble-metal-free Mo<sub>2</sub>C-In<sub>2</sub>S<sub>3</sub> heterojunction photocatalyst with efficient charge separation for enhanced photocatalytic H<sub>2</sub> evolution under visible light," *Journal of Colloid and Interface Science*, vol. 582, pp. 488–495, 2021.
- [35] Z. W. Fang, D. Fernandez, N. N. Wang, Z. C. Bai, and G. H. Yu, "Mo<sub>2</sub>C@3D ultrathin macroporous carbon realizing efficient and stable nitrogen fixation," *Science China Chemistry*, vol. 63, no. 11, pp. 1570–1577, 2020.
- [36] R. G. Ma, Y. Zhou, Y. F. Chen, P. X. Li, Q. Liu, and J. C. Wang, "Ultrafine molybdenum carbide nanoparticles composited with carbon as a highly active hydrogen-evolution electrocatalyst," *Angewandte Chemie International Edition*, vol. 127, no. 49, pp. 14936–14940, 2015.
- [37] Y. Jiang, H. Y. Chen, J. Y. Li et al., "Z-scheme 2D/2D heterojunction of CsPbBr<sub>3</sub>/Bi<sub>2</sub>WO<sub>6</sub> for improved photocatalytic CO<sub>2</sub> reduction," *Advanced Functional Materials*, vol. 30, no. 50, article 2004293, 2020.
- [38] J. F. Liu, P. Wang, J. J. Fan, H. G. Yu, and J. G. Yu, "In situ synthesis of Mo<sub>2</sub>C nanoparticles on graphene nanosheets for enhanced photocatalytic H<sub>2</sub>-production activity of TiO<sub>2</sub>," *ACS Sustainable Chemistry & Engineering*, vol. 9, no. 10, pp. 3821–3830, 2021.
- [39] L. Wang, Y. K. Li, C. Wu, X. Li, G. S. Shao, and P. Zhang, "Tracking charge transfer pathways in SrTiO<sub>3</sub>/CoP/Mo<sub>2</sub>C nanofibers for enhanced photocatalytic solar fuel production," *Chinese Journal of Catalysis*, vol. 43, no. 2, pp. 507–518, 2022.
- [40] C. S. Lei, W. Zhou, Q. G. Feng et al., "Charge engineering of Mo<sub>2</sub>C@defect-rich N-doped carbon nanosheets for efficient electrocatalytic H<sub>2</sub> evolution," *Nano-Micro Letters*, vol. 11, no. 1, pp. 1–10, 2019.
- [41] J. F. Wang, L. L. Zhao, M. C. Wang, and S. C. Lin, "Molecular insights into early nuclei and interfacial mismatch during vapor deposition of hybrid perovskites on titanium dioxide substrate," *Crystal Growth & Design*, vol. 17, no. 12, pp. 6201–6211, 2017.
- [42] Z. Fan, H. Xiao, Y. L. Wang et al., "Layer-by-layer degradation of methylammonium lead tri-iodide perovskite microplates," *Joule*, vol. 1, no. 3, pp. 548–562, 2017.
- [43] X. W. Shi, M. Fujitsuka, S. Kim, and T. Majima, "Faster electron injection and more active sites for efficient photocatalytic H<sub>2</sub> evolution in g-C<sub>3</sub>N<sub>4</sub>/MoS<sub>2</sub> hybrid," *Small*, vol. 14, no. 11, article 1703277, 2018.
- [44] X. Z. Yue, S. S. Yi, R. W. Wang, Z. T. Zhang, and S. L. Qiu, "Well-controlled SrTiO<sub>3</sub>@Mo<sub>2</sub>C core-shell nanofiber photocatalyst: boosted photo-generated charge carriers transportation and enhanced catalytic performance for water reduction," *Nano Energy*, vol. 47, pp. 463–473, 2018.
- [45] C. Aprile, A. Corma, and H. Garcia, "Enhancement of the photocatalytic activity of TiO<sub>2</sub> through spatial structuring and particle size control: from subnanometric to submillimetric length scale," *Physical Chemistry Chemical Physics*, vol. 10, no. 6, pp. 769–783, 2008.
- [46] Y. Kumar, K. C. Sanal, T. D. Perez, N. R. Mathews, and X. Mathew, "Band offset studies in MAPbI<sub>3</sub> perovskite solar cells using X-ray photoelectron spectroscopy," *Optical Materials*, vol. 92, pp. 425–431, 2019.
- [47] E. S. Thibau, A. Llanos, and Z. H. Lu, "Disruptive and reactive interface formation of molybdenum trioxide on organometal trihalide perovskite," *Applied Physics Letters*, vol. 110, no. 8, article 081604, 2017.
- [48] S. Jin, Z. H. Shi, H. J. Jing et al., "Mo<sub>2</sub>C-MXene/CdS heterostructures as visible-light photocatalysts with an ultrahigh hydrogen production rate," *ACS Applied Energy Materials*, vol. 4, no. 11, pp. 12754–12766, 2021.
- [49] W. Cui, N. Y. Cheng, Q. Liu, C. J. Ge, A. M. Asiri, and X. P. Sun, "Mo<sub>2</sub>C nanoparticles decorated graphitic carbon sheets: biopolymer-derived solid-state synthesis and application as an efficient electrocatalyst for hydrogen generation," *ACS Catalysis*, vol. 4, no. 8, pp. 2658–2661, 2014.
- [50] H. W. Huang, B. Pradhan, J. Hofkens, M. B. J. Roeffaers, and J. A. Steele, "Solar-driven metal halide perovskite photocatalysis: design, stability, and performance," *ACS Energy Letters*, vol. 5, no. 4, pp. 1107–1123, 2020.
- [51] B. J. Ma, H. J. Xu, K. Y. Lin et al., "Mo<sub>2</sub>C as non-noble metal co-catalyst in Mo<sub>2</sub>C/CdS composite for enhanced photocatalytic H<sub>2</sub> evolution under visible light irradiation," *ChemSusChem*, vol. 9, no. 8, pp. 820–824, 2016.

- [52] Y. Yang, X. B. Xu, and X. Wang, "Synthesis of Mo-based nanostructures from organic-inorganic hybrid with enhanced electrochemical for water splitting," *Science China Materials*, vol. 58, no. 10, pp. 775–784, 2015.
- [53] J. W. Fang, H. Q. Fan, Y. Ma, Z. Wang, and Q. Chang, "Surface defects control for ZnO nanorods synthesized by quenching and their anti-recombination in photocatalysis," *Applied Surface Science*, vol. 332, pp. 47–54, 2015.
- [54] B. C. Qiu, Q. H. Zhu, M. M. Du, L. G. Fan, M. Y. Xing, and J. L. Zhang, "Efficient solar light harvesting CdS/Co<sub>9</sub>S<sub>8</sub> hollow cubes for Z-scheme photocatalytic water splitting," *Angewandte Chemie International Edition*, vol. 56, no. 10, pp. 2684–2688, 2017.
- [55] S. Nayak, L. Mohapatra, and K. Parida, "Visible light-driven novel g-C<sub>3</sub>N<sub>4</sub>/NiFe-LDH composite photocatalyst with enhanced photocatalytic activity towards water oxidation and reduction reaction," *Journal of Materials Chemistry A*, vol. 3, no. 36, pp. 18622–18635, 2015.
- [56] B. Ma, J. P. Zhao, Z. H. Ge, Y. T. Chen, and Z. H. Yuan, "5 nm NiCoP nanoparticles coupled with g-C<sub>3</sub>N<sub>4</sub> as high-performance photocatalyst for hydrogen evolution," *Science China Materials*, vol. 63, no. 2, pp. 258–266, 2020.
- [57] H. W. Huang, L. Y. Liu, Y. H. Zhang, and N. Tian, "One pot hydrothermal synthesis of a novel Bi<sub>2</sub>MoO<sub>6</sub>/Bi<sub>2</sub>WO<sub>6</sub> heterojunction photocatalyst with enhanced visible-light-driven photocatalytic activity for rhodamine B degradation and photocurrent generation," *Journal of Alloys and Compounds*, vol. 619, pp. 807–811, 2015.
- [58] D. D. Ma, J. W. Shi, L. Sun et al., "Knack behind the high performance CdS/ZnS-NiS nanocomposites: optimizing synergistic effect between cocatalyst and heterostructure for boosting hydrogen evolution," *Chemical Engineering Journal*, vol. 431, article 133446, 2022.
- [59] G. T. Sun, J. W. Shi, S. M. Mao et al., "Dodecylamine coordinated tri-arm CdS nanorod wrapped in intermittent ZnS shell for greatly improved photocatalytic H<sub>2</sub> evolution," *Chemical Engineering Journal*, vol. 429, article 132382, 2022.
- [60] S. M. Mao, J. W. Shi, G. T. Sun et al., "Cu (II) decorated thiol-functionalized MOF as an efficient transfer medium of charge carriers promoting photocatalytic hydrogen evolution," *Chemical Engineering Journal*, vol. 404, article 126533, 2021.
- [61] L. L. Deng, H. J. Yang, R. H. Pan et al., "Achieving 20% photovoltaic efficiency by manganese doped methylammonium lead halide perovskites," *Journal of Energy Chemistry*, vol. 60, pp. 376–383, 2021.
- [62] Z. S. Hu, Z. H. Lin, J. Su, J. C. Zhang, J. J. Chang, and Y. Hao, "A review on energy band-gap engineering for perovskite photovoltaics," *Solar RRL*, vol. 3, no. 12, article 1900304, 2019.
- [63] M. X. Li, Y. Zhu, H. Y. Wang, C. Wang, N. Pinna, and X. F. Lu, "Ni strongly coupled with Mo<sub>2</sub>C encapsulated in nitrogen-doped carbon nanofibers as robust bifunctional catalyst for overall water splitting," *Advanced Energy Materials*, vol. 9, no. 10, article 1803185, 2019.
- [64] S. J. Li, Z. Y. Zhang, C. Xu et al., "Magnetic doping induced superconductivity-to-incommensurate density waves transition in a 2D ultrathin Cr-doped Mo<sub>2</sub>C crystal," *ACS Nano*, vol. 15, no. 9, pp. 14938–14946, 2021.